J. Synchrotron Rad. (1996). **3**, 65–74

Feasibility and Realization of Single-Pulse Laue Diffraction on Macromolecular Crystals at ESRF

D. Bourgeois,[a,b] T. Ursby,[a] M. Wulff,[a] C. Pradervand,[c] A. Legrand,[c] W. Schildkamp,[c] S. Labouré,[a] V. Srajer,[c] T. Y. Teng,[c] M. Roth[b] and K. Moffat[c]

[a]ESRF, BP 220, 38043 Grenoble CEDEX, France, [b]UPR 9015/IBS, 41 Avenue des Martyrs, 38027 Grenoble CEDEX 1, France, and [c]Department of Biochemistry and Molecular Biology, and the Consortium for Advanced Radiation Sources, University of Chicago, 920 East 58th Street, Chicago, IL 60637, USA. E-mail: bourgeoi@esrf.fr

(*Received 30 October 1995; accepted 11 December 1995*)

Laue diffraction patterns with an exposure time of *ca* 60 ps have been acquired at the European Synchrotron Radiation Facility (ESRF) on protein crystals by using the single-bunch mode of the storage ring. A 10 ns laser pulse initiating photodissociation was synchronized with the X-ray pulse. The potential for a quantitative detection of conformational changes in proteins on the nanosecond timescale with this technique is demonstrated using the example of carbonmonoxymyoglobin, from simulations and real data. The instrumental aspects of the experiment (highly intense X-ray beam, fast shutter system, Laue camera, detector, laser apparatus and synchronization technique) are emphasized.

Keywords: protein crystallography; Laue diffraction; time-resolved studies; instrumentation; carbonmonoxymyoglobin.

1. Introduction

Transient structural modifications in proteins associated with the build up of short-lived intermediates during catalysis or substrate binding are becoming more widely studied, as they reveal how three-dimensional structure has been designed by nature to effect protein function (Cruickshank, Helliwell & Johnson, 1992, and references therein). However, most tertiary structural changes occur at physiological temperatures in the millisecond to nanosecond timescale, and the only way so far of observing these changes with X-rays has been to slow down reaction rates artificially in order to match the lifetime of intermediates with the data collection time from standard diffraction techniques. Several biochemical methods have been developed to produce slow substrates or less reactive mutants (Pai, 1992; Bolduc *et al.*, 1995), and cryocrystallography has proved extremely useful (Schlichting, Berendzen, Phillips & Sweet, 1994; Teng, Srajer & Moffat, 1994). Unfortunately, these techniques run the risk of trapping an enzymatic reaction in an abnormal state (Moffat, 1989; Moffat & Henderson, 1995), and the validity of intermediate structures must be carefully assessed.

With the advent of third-generation synchrotron radiation sources, such as the ESRF, APS and SPring8, that provide X-ray beams of reduced angular divergence and extremely high brilliance, the accessible timescales can now be lowered to the lifetime of the transient species involved in protein dynamics at physiological temperatures. Fast sample rotation and large angle oscillation techniques could lower the accessible timescale down to the millisecond range with monochromatic radiation (Hajdu & Andersson, 1993; Weisgerber & Helliwell, 1993). However, the Laue technique is the only method presently able to provide valuable information on faster timescales. The wide bandwidth and smoothness of synchrotron X-ray spectra have led to a renewal of this old technique (Moffat, Szebenyi & Bilderback, 1984; Helliwell *et al.*, 1989), which has recently been used successfully (see, for example, Hajdu *et al.*, 1987; Schlichting, Almo *et al.*, 1990; Singer, Smalås, Carty, Mangel & Sweet, 1993; Fülop *et al.*, 1994; Bolduc *et al.*, 1995). In this technique, diffraction occurs simultaneously from all lattice planes fulfilling the Bragg condition for some wavelength present in the incident X-ray beam, resulting in a considerable gain in acquisition speed. No crystal rotation or oscillation is required. New processing methods now address the complications inherent in the principles of Laue diffraction (spatial and harmonic overlaps, wavelength normalization, low-resolution hole, high sensitivity to mosaic spread), and crystallographic data of quality comparable to those obtained with oscillation techniques have been obtained (Ren & Moffat, 1994, 1995*a*,*b*).

In using the Laue technique one can take advantage of the temporal structure of synchrotron radiation sources (Mills, 1991). The single-bunch mode of operation of a synchrotron ring is of particular interest. Firstly, it gives the highest attainable instantaneous power on the sample; secondly, it permits with relative ease the isolation of a single X-ray pulse with a mechanical shutter; and thirdly, it usually produces Laue patterns free of radiation damage, since the latter, if present, propagates through the crystal

over times longer than 100 ps. That is, the information is recorded before radiation damage occurs (although irreversible radiation damage will eventually accumulate). At the ESRF, as a consequence of a small beam emittance and a low momentum compaction factor (a characteristic feature of third-generation sources), X-ray pulses as short as *ca* 60 ps FWHM are produced in the single-bunch mode, and this establishes the minimum exposure time of our Laue images. Therefore, provided adequate instrumental methods, detectors and processing techniques can be developed, one can approach the challenging task of solving the three-dimensional structure of short-lived intermediates building up on the milli, micro and even 100 ps timescale. However, the success of such experiments relies primarily on biochemical techniques that allow the simultaneous and uniform triggering of a transient process in all molecules of a crystal. Concentration, temperature, pressure or pH jumps (Clifton *et al.*, 1991) might be used to start a reaction, but the fastest timescales seem to be obtainable only by laser techniques that allow ligand photolysis or photochemical activation of caged compounds. It must also be kept in mind that although the Laue method stimulates a large portion of reciprocal space (depending on crystal symmetry) in a single shot, complete coverage with sufficient redundancy usually necessitates several exposures. It is thus considerably easier to study reversible reactions, where a single crystal (sufficiently radiation-hard) can be used to record many Laue patterns.

This paper describes the instrumentation developed at the white-beam station (BL3) at the ESRF to record Laue patterns in synchronization with a pulsed nanosecond laser that triggers photoactivation in the sample. Diffraction images are obtained by using either the X-rays emitted by a single electron bunch (60 ps FWHM, ESRF single-bunch mode, 5–15 mA) or by an electron 'superbunch' (1 μs pulse, ESRF one-third filling mode, 150 mA). Photodissociation of substrates or caged compounds is obtained with a YAG/dye laser system synchronized with the ESRF bunch clock. The feasibility of single-pulse Laue diffraction on protein crystals has already been demonstrated (Szebenyi *et al.*, 1992), though only very limited data could be obtained. Related instrumentation has been described for time-resolved experiments on a longer timescale and/or using different X-ray techniques (Mills, Larson, White & Noggle, 1983; Mills, Lewis, Harootunian, Huang & Smith, 1984; Bartunik, 1983; Moffat, Chen, Ng, McRee & Getzoff, 1992). However, the possibility of routinely acquiring high-quality single-pulse Laue data sets with a broad bandpass (0.35–1.75 Å) is a new development (Bourgeois *et al.*, 1995).

Before designing complex instrumentation, it is essential to show that the photon flux available from a single pulse at ESRF is expected to permit an unambiguous detection of small conformational changes in proteins with the Laue technique. This aspect is demonstrated by carrying out simulations and a statistical study of experimental data on carbonmonoxymyoglobin, a molecule still under active study by a variety of techniques (Franzen, Bohn, Poyart & Martin, 1995; Hagen, Hofrichter & Eaton, 1995; Lim, Jackson & Anfinrud, 1995).

2. X-ray beam

The 6 GeV ESRF storage ring can be operated in a dedicated single-bunch mode (5–15 mA machine current, horizontal emittance 7 nm mrad with 1.5% coupling). In this mode, 62 ps (FWHM) X-ray pulses are delivered at a frequency of 355.0423 kHz. X-rays are generated by a 45-pole hybrid wiggler operated at 20.1 mm gap [source size: 0.33 (horizontal) × 0.12 (vertical) mm^2; critical energy: 20.0 keV]. A platinum-coated toroidal graphite mirror was used at an incidence angle of 3.12 mrad to focus the beam both vertically and sagittally, with a demagnification factor $M = 0.62$. The insertion device and the optics on BL3 were designed for optimal power density of the focal spot (Wulff, 1992). With a machine current of 15 mA, 1.0×10^{10} photons can be delivered on a $0.2 \times 0.2\ mm^2$ sample, in a single 60 ps pulse and over a bandwidth extending from 7 to 35 keV. Likewise, the spectral flux at 16 keV is 1.0×10^7 photons $(0.2 \times 0.2\ mm^2)^{-1}$ $(0.1\%\ \text{bandwidth})^{-1}$.

The beam crosses several absorbing elements before reaching the sample: 2 × 0.130 mm carbon windows (front-end prefilters), 2 × 0.5 mm beryllium windows (front end and pipe exit), 1 mm carbon (additional filter to minimize radiation damage on the sample), and 1.3 m of air. The theoretical X-ray spectrum predicted at the sample position is plotted in Fig. 1 (solid line). The instantaneous power on a $0.2 \times 0.2\ mm^2$ sample during a single-pulse exposure reaches 0.6 MW and the energy absorbed by a typical 0.2 mm thick myoglobin crystal is 60 μJ. The X-ray spectrum as seen by the detector (owing to the presence

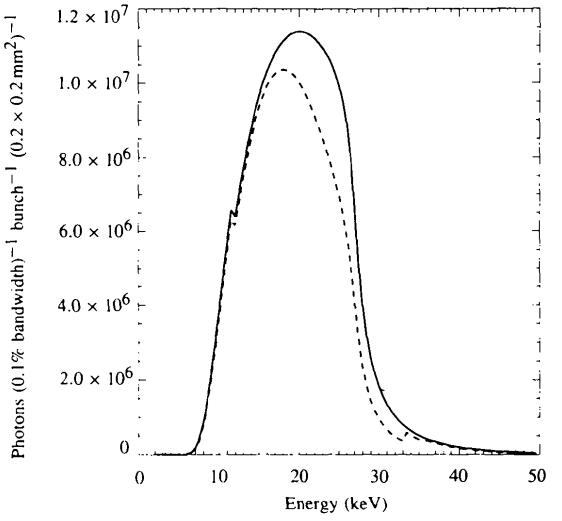

Figure 1
Theoretical X-ray spectrum calculated at the sample position (solid line), and theoretical spectrum as seen by the detector (dashed line).

of a 0.5 mm beryllium input window, and to incomplete absorption in the CsI:Na scintillator at short wavelength, see §3.2) is also shown in Fig. 1 (dashed line). By two-dimensional scanning of a 20 × 5 μm^2 slit located at the sample position, it is possible to reconstruct a two-dimensional profile of the X-ray beam, as shown in Fig. 2. The beam FWHMs are 210 and 290 μm in the horizontal and vertical directions, respectively, in agreement with the known mirror aberrations and imperfections.

A layout of the beamline in the Laue configuration is illustrated in Fig. 3.

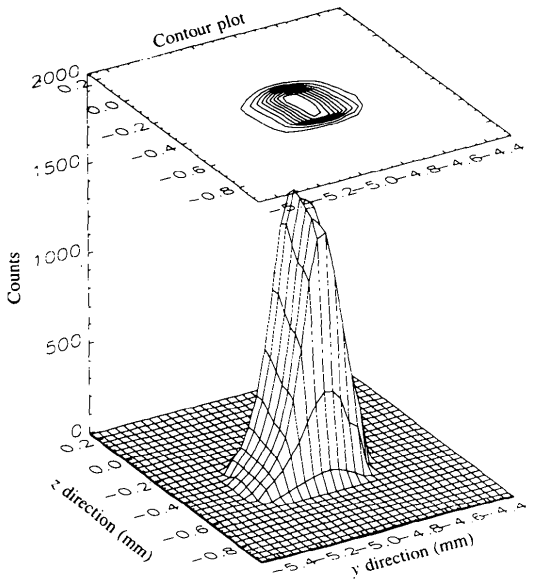

Figure 2
Two-dimensional experimental X-ray beam profile at the sample position. This beam profile was obtained by using the high-energy part of the X-ray spectrum. Profiles may vary slightly as a function of X-ray wavelength.

3. Instrumentation

3.1. *Shutter assembly*

The key elements of the Laue camera consist of three X-ray shutters mounted in series.

The first shutter is a water-cooled copper block operated by pneumatic pressure. It is used to protect the downstream elements of the camera from excessive heat load. The minimum opening time of this pre-shutter is *ca* 50 ms.

The second shutter is an ultrafast chopper wheel developed by LeGrand and colleagues (LeGrand, Schildkamp & Blank, 1989; LeGrand, Pradervand & Schildkamp, 1996), which is open to X-rays for 3.7 μs every 2.25 ms. This 127 mm diameter titanium chopper is traversed along its diameter by a 0.79 (horizontal) × 0.65 (vertical) mm^2 channel (offset from the rotation axis by 7.6 mm), and rotates at a frequency of 445 Hz, asynchronously with the X-ray clock. As a result of the significant horizontal divergence of the X-ray beam (1.22 mrad) and the limited horizontal aperture of the chopper channel, it is essential to position the chopper as close as possible to the sample (Fig. 3) in order to minimize the clipping of the beam. The opening profile of the chopper is of trapezoidal shape, as a consequence of the chopper geometry and finite vertical beam size. The profile was measured experimentally with an X-ray beam similar to the one shown in Fig. 2. It was acquired with an avalanche diode located at the sample position (see §3.4) and a fast digital oscilloscope operated in persistence mode. By taking advantage of the asynchronicity between the X-ray clock and the chopper-rotation frequency, X-ray pulses 'sweep' through the chopper-opening profile and progressively reconstruct it. The result is shown in Fig. 4 and compared with a theoretical opening profile assuming a beam of Gaussian shape (FWHM = 300 μm). The discrepancy between the two profiles can be explained by (i) the experimental beam profile deviating from a Gaussian shape and (ii) a saturation of the diode response,

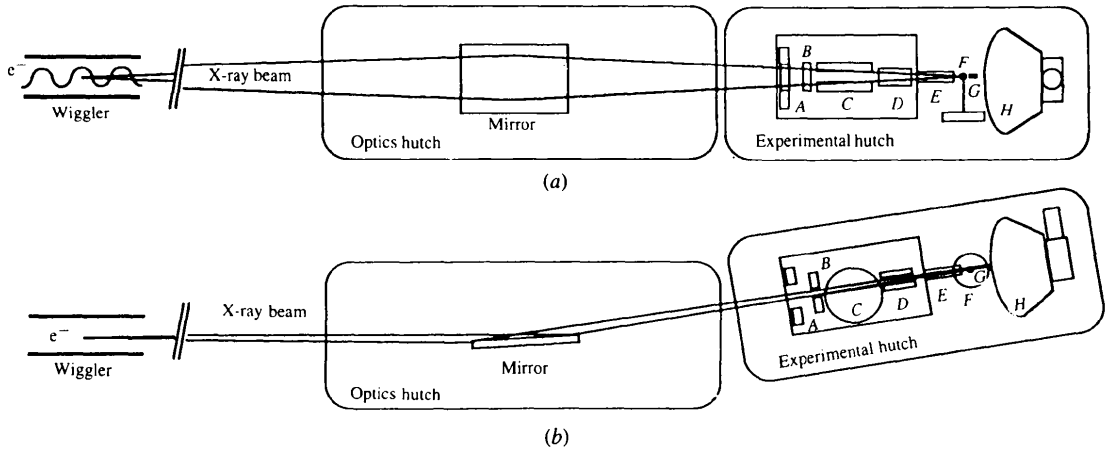

Figure 3
Sketch of the beamline and Laue camera: *A*, water-cooled heat-load shutter; *B*, 300 μm entrance slit; *C*, chopper wheel; *D*, magnetic shutter; *E*, beam guard; *F*, sample; *G*, tungsten beam stop; *H*, XRII detector. (*a*) Top view, (*b*) side view.

which tends to flatten the top part of the experimental profile.

A digital electronics board was designed to predict, ahead of time, instants when the center of the chopper-opening function will coincide with the passage of an X-ray pulse (LeGrand, Pradervand & Schildkamp, 1996). If this feature is neglected, one or even two partially chopped pulses might be selected rather than only a full one. By recording a pickup signal from the wheel, the board monitors the drift of the chopper phase relative to the X-ray clock. On the assumption that the chopper speed remains constant over periods of time comparable to its rotation period, the time of matching can be predicted one rotation period (2.247 ms) in advance. A mismatch of the wheel phase can be accepted within a certain tolerance, given by the duration of the top flat part of the chopper-opening profile (Fig. 4).

The delay of 2.247 ms is long enough to open the third shutter, a magnetic solenoid (Fig. 3). This shutter is based on a 0.38 mm thick steel blade coated with 0.25 mm of tungsten, which intercepts the X-ray beam at 83° grazing incidence. Its minimum opening time is *ca* 1.3 ms and it can therefore be closed before the next opening of the chopper, allowing the overall selection of only one X-ray pulse to reach the sample.

During a typical opening window of the preshutter of 500 ms, the rejection factor of the two downstream shutters exceeds 10^8. The three shutters and a 300 μm vertical slit positioned upstream of the chopper to clean up the beam are enclosed hermetically in a lead house.

3.2. *Detector*

Images were recorded with an X-ray image intensifier (XRII) coupled to a slow-scan CCD camera. The XRII, developed by the ESRF detector group in collaboration with Thomson Tubes Electronics (Moy, 1994) was designed to cover the energy range 5–80 keV. The detector consists of a large vacuum vessel closed with a 0.5 mm thick beryllium window transparent to X-rays. A 0.225 mm thick CsI:Na layer covered by a photocathode converts the X-ray image into electrons. Electrodes focus the electron image onto a high-resolution-output P20 phosphor screen, which in turn produces a visible image on a 1152 × 1242 CCD chip through a suitable optical relay system. The signal is then digitized to 16 bits at a rate of 150 kHz. This detector possesses the following advantages over image plate systems:

(i) High detective quantum efficiency at low signal level (greater than 50% between 5 and 25 keV) in the energy bandwidth of interest.

(ii) Conversion efficiency optimization by tuning the iris of the optical system, which allows a match between the dynamic range of the detector and the Laue signal intensity. In the case of single-pulse exposures where many Laue spots contain only a few photons, this tunability is a key advantage. It allows the contribution from dark current and readout noise intrinsic to the detector (*ca* 15 e^-, equivalent to *ca* 3 ADU $pixel^{-1}$) to be minimized. However, the presence of a large gain of the order of 50 ADU $photon^{-1}$ at 20 keV, which is also proportional to X-ray energy and thus affects a diffraction peak in a different manner than its underlying X-ray background, must be taken into account during data processing. Care must be taken not to overestimate the quality of the Laue images.

(iii) Synchronization of the CCD shutter and CCD read-out by external triggering. This feature, by keeping the CCD exposure time to a minimum, precludes any accumulation on the image of diffuse X-ray noise present in the experimental hutch as soon as the main beamline shutter is opened. Two precautions have to be taken. Firstly, the proper minimum exposure time of the CCD is determined by the time decay of the P20 phosphor. It was found that 15 ms is satisfactory. Secondly, the CCD shutter takes *ca* 10 ms to open fully from center to edges. Therefore, it must be triggered at least this amount of time ahead of the X-ray flash, a situation which is not compatible with the fact that the chopper electronics board is only able to predict the latter 2.25 ms in advance. Another method is preferred, which consists of opening the CCD shutter a long time in advance and of continuously erasing the CCD chip until 2 ms before the X-ray pulse.

Despite these significant advantages, the XRII/CCD detector has the following drawbacks:

(i) Although the spatial resolution is of comparable or better quality than from image-plate systems (point-spread function: 300 μm at FWHM, 1.5 mm at 0.1% of maximum), the sensitive area is limited to 15 × 17 cm^2, which imposes the choice of a less than optimal crystal-to-detector distance.

(ii) The presence of a strongly convex input window results in severe spatial distortions of the data, which are corrected for in a later stage with the package *FIT2D* (Hammersley, Svensson & Thompson, 1994).

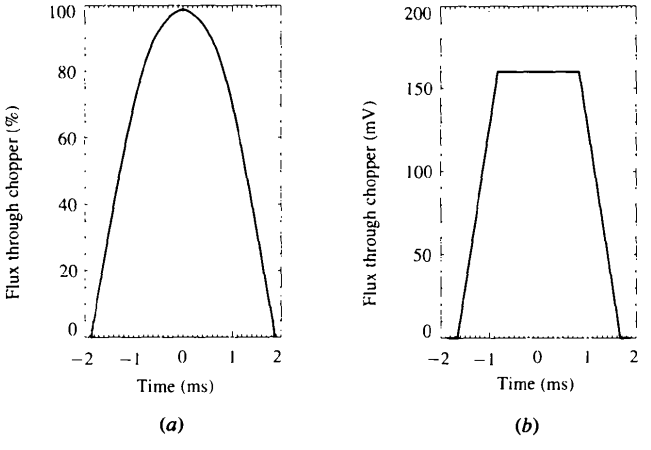

Figure 4
Predicted (*a*) and (contour of the) experimental (*b*) opening profiles of the chopper wheel. The vertical scale in (*a*) is arbitrary.

(iii) The electron paths in the vacuum vessel of the detector are strongly affected by the presence of surrounding magnetic fields, and the use of a specially designed mu-metal magnetic shielding is mandatory.

(iv) Differential sensitivity of the CsI:Na layer, and differential absorption through the input beryllium window as a function of X-ray incidence angle and energy, produce severe deviations from a uniform response of the detector over its sensitive area. These deviations are partially corrected by recording a flood-field image with a strontium-doped glass sample producing an isotropic fluorescence emission (Moy *et al.*, 1996). Only Laue reflections stimulated by wavelengths close to the fluorescence wavelength can be accurately corrected in this way.

3.3. *Nd:YAG/dye laser system*

Ligand photodissociation of crystals is obtained with a tunable dye laser (Continuum ND60) pumped by the second harmonic (540 nm) of a neodymium:yttrium aluminium garnet (Nd:YAG) laser (Continuum NY61-10). The YAG laser flashlamp is externally triggered at 10 Hz to ensure thermal equilibrium. 10 ns wide laser pulses are obtained by cavity Q switching, 340 µs after flashlamp excitation. Larger delays between flashlamp excitation and Q switching result in attenuated and unstable pulse intensity as well as longer pulse duration. With a DCM 630 dye, 38 mJ pulses (peak power: 3.8 MW) are produced. The light is brought to the sample position *via* a 900 µm diameter silicon multimode fiber and using input and output focusing lenses. Pulses up to 13 mJ (corresponding to an instantaneous power of 1.6 MW) can be delivered over an area of *ca* 0.5 mm^2.

Tunability of the dye laser is essential in order to stimulate crystals at a wavelength at which their optical density is low, thus ensuring uniform photochemical stimulation and minimizing the generation of longitudinal thermal gradients.

3.4. *Monitoring device*

Timing of the experiment is controlled with a large-area (7 mm^2 sensitive layer) avalanche diode (S2384, Hamamatsu), coupled to a high-frequency preamplifier and a 500 MHz LeCroy digital oscilloscope. It has been established previously (Kishimoto, 1991) that such a device can be used as an X-ray detector. In our case, the diode is positioned close to the sample position (about 20 mm away from the beam axis) and records the elastic/inelastic scattering from the sample and the glass capillary, without perturbing the diffraction experiment. The diode is used without removing its protective glass window, and is mostly sensitive to X-rays of energy comparable to the critical energy of the insertion device. In practice, 5 ns wide pulses of a few hundreds of millivolts amplitude are recorded with a 50 Ω load impedance. The diode is used to check the phase difference between the ESRF X-ray clock and the actual arrival of X-rays at the chopper position, and during experiments to control the purity and the intensity of the X-ray flash impinging on the sample. In addition, the device is able to record diffuse scattered laser light, so the exact delay between the laser pulse and the X-ray pulse can easily be controlled. Fig. 5 shows a pattern recorded with this avalanche diode, where the laser and X-ray flashes are separated by 17 ± 1 ns.

3.5. *Synchronization*

In order to pump the sample with a laser flash and to probe it at the appropriate time (chosen by the user) by an X-ray flash, it is necessary to bring three asynchronous clocks together in phase. These clocks are:

(i) the X-ray clock [ESRF master radio-frequency clock (352.2020 MHz)/992], at 355.0423 kHz,

(ii) the chopper rotation frequency (445 Hz, average value from the chopper LED), and

(iii) the laser flashlamp triggering clock (10 Hz, from a standard function generator).

Four timing units are combined to handle the timing sequence:

(i) Two units, called VPDU1 and VPDU2 (VME Programmable Delay Unit, developed at the ESRF), provide tunable delay lines: from an input trigger signal (generated either by software, or by hardware), the module generates a series of TTL output pulses, whose delays and durations are programmed *via* a computer interface by the user.

(ii) The chopper control VME module (see §3.1) predicts phase coincidence between the X-ray clock and the chopper opening time. From a triggering signal, the module generates an output TTL pulse 2.25 ms before the matching condition is met.

(iii) Finally, a home-made logic module links both VPDUs and the chopper module.

A complete timing diagram is shown in Fig. 6. In order to create a phase-matching condition between the

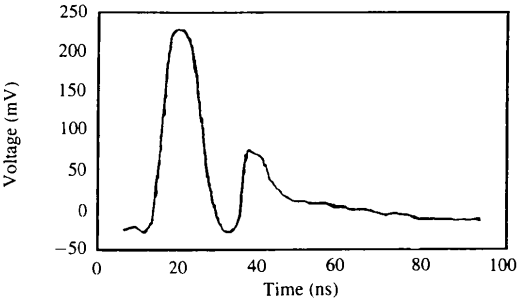

Figure 5
Monitoring signal recorded by the avalanche diode. The laser pulse is separated from the X-ray pulse by 17 ns. LeCroy digital oscilloscope, 20 ns division^{-1} (horizontal), 100 mV division^{-1} (vertical). The exact delay between the laser and the X-ray pulse is measured between the center of the laser pulse and the beginning of the X-ray pulse. The finite width of the X-ray pulse (which should be a δ function on this time scale) arises from the response function of the detector and electronics.

three clocks, the 10 Hz laser flashlamp triggering clock is momentarily disabled (during *ca* 500 ms) and replaced by one pulse from VPDU2 at a time determined by the delay of interest between the X-ray and laser flashes. A second pulse from VPDU2 triggers Q switching of the laser cavity approximately 340 μs later. The exact value of this delay must take into account unpredictable but reproducible effects like cable propagation time, and is determined experimentally from the signal recorded with the avalanche diode. The main task of the logic module is to ensure that the added flashlamp triggering pulse is separated from the preceding and following pulses (delivered by the 10 Hz clock) by more than 100 ms. If this is not the case (due to an excessively long prediction time from the chopper control module), the logic board disables VPDU2 and the experiment fails, a situation that in practice never happens. This precaution is necessary to prevent damaging the laser flashlamp with an excessive repetition rate. The laser firing jitter was found to be less than 2 ns. VPDU2 is also used to start the detector as soon as an X-ray pulse is predicted, and to trigger a digital oscilloscope at the predicted time of the X-ray flash in order to check the presence of the signal from the avalanche diode.

The whole timing sequence is triggered by software and can be easily combined or looped with crystal rotation, such that a whole data set can be collected automatically in a few minutes.

4. Feasibility of the experiment

Based on precise calculations (see §2) of the X-ray flux impinging on a macromolecular crystal of realistic dimensions in a single pulse, we performed simulations to determine if the statistical accuracy of Laue data likely to be obtained at BL3 would allow the detection of the small intensity variations associated with structural modifications

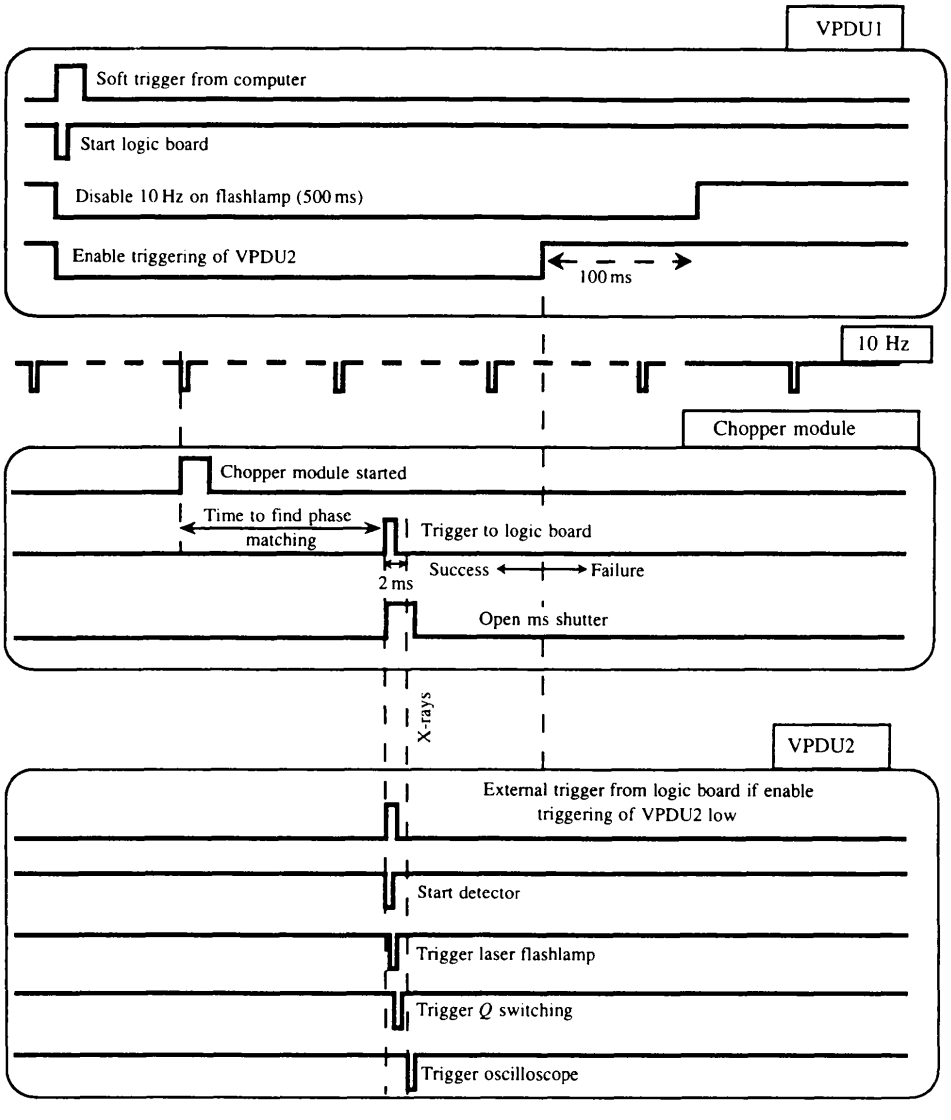

Figure 6
Timing sequence for laser–X-ray synchronization.

of a protein sample. In these simulations we used the atomic models of carbonmonoxymyoglobin (MbCO) and photolysed myoglobin (Mb*) refined from monochromatic data acquired at 40 K (molecular weight: 17.8 kDa; crystallizes in space group $P2_1$; unit cell: a = 64.6, b = 31.10, c = 34.80 Å, β = 105.5°) (Teng, Srajer & Moffat, 1994). Integrated intensities of Laue reflections were calculated with the local program *SLIP* (Simulation of Laue Intensity Patterns) for a chosen crystal orientation and with the resolution limit set to 2.2 Å. The following formula of practical interest was used (derived from Warren, 1969):

$$I(\mathbf{h}, \lambda)_{\text{sim}} = 98\, g_0\, I_0(\lambda)\lambda^2 F^2(\mathbf{h})(V/V_0^2)PLA(\lambda)D(\lambda) \quad (1)$$

where I_{sim} [ADU pulse^{-1}] is the simulated integrated intensity as recorded by the detector, g_0 [ADU keV^{-1}] is the detector gain, I_0 [photons pulse^{-1} mm^{-2} (0.1% bandwidth)$^{-1}$] is the incident flux on the sample, λ [Å] is the wavelength, F [electrons (unit cell)$^{-1}$] is the structure-factor amplitude for the reflection **h**, V [mm^3] is the crystal volume and V_0 [Å^3] the unit-cell volume, P [no units] is the beam polarization factor, $L = (2\sin^2\theta)^{-1}$ [no units] the Lorentz factor, θ is the Bragg angle, A [%] the absorption through the sample and the air path between the sample and detector, and finally D [%] is the quantum efficiency of the detector. The factor λ^2 (and not λ^4) in (1) results from the fact that $I_0(\lambda)$ is expressed in units of fractional bandwidth and that the detector gain for a given reflection is proportional to the X-ray energy. The numerical factor in (1) takes into account the Thompson scattering length and the units used. In a second step, all reflections were assigned a standard deviation based on Poissonian statistics, and on a realistic assessment of the X-ray background and detector noise:

$$\sigma_I(\mathbf{h}, \lambda)_{\text{sim}} = \{[I(\mathbf{h}, \lambda) + nb]/DQE\}^{1/2} \quad (2)$$

where DQE [no units] is the detective quantum efficiency of the detector (assumed to be wavelength independent and taken as 0.5), n [no units] is the number of pixels in the detector covering the diffraction peak and b [ADU pulse^{-1}] corresponds to the number of X-ray photons collected in a single pixel:

$$b = \int_{\lambda} g_0 I_0(\lambda)\left[\sum_i D(\sigma^i_{\text{elas}} + \sigma^i_{\text{inelas}}, \lambda, d_i)\right]\Omega_{\text{pix}} S\, \frac{1.24\times10^4}{\lambda^2}\, \mathrm{d}\lambda \quad (3)$$

where σ^i_{elas}, σ^i_{inelas} and d_i are the elastic cross section, inelastic cross section and effective thickness of the ith diffusing material (100 mm of air, 0.2 mm of myoglobin and 0.05 mm of silica forming the capillary in our case), D is the percentage of diffused X-rays at wavelength λ and over a solid angle 4π, Ω is the solid angle subtended by a single detector pixel positioned at the correct distance from the sample, and S [mm^2] is the beam cross section. The factor $1.24 \times 10^4/\lambda^2$ results from the units used. Anisotropy in inelastic scattering, diffuse scattering produced by partially ordered elements such as water in the sample and additional background noise originating from elsewhere in the beamline hutch (slits, windows, shutters or air paths) were ignored. The X-ray background calculated in this way amounts to an average of 7.5 photons of mean energy 15.5 keV in a 100 µm^2 pixel located at 170 mm from the sample.

In a second stage, the simulated accuracy of the data $\sigma_I(\mathbf{h}, \lambda)_{\text{sim}}/I(\mathbf{h}, \lambda)_{\text{sim}}$ was compared with the relative intensity change $\Delta I(\mathbf{h}, \lambda)_{\text{sim}}/I(\mathbf{h}, \lambda)_{\text{sim}}$ expected from the structural differences between the low-temperature models for MbCO and Mb*. Values were averaged over resolution bins. As can be seen in Fig. 7, the intensity changes between MbCO and Mb* are slightly lower than the standard deviations of the measurements, but are uniformly distributed with resolution. Since the difference signal in real space is expected to contain substantial features in the vicinity of the heme pocket, a satisfactory signal-to-noise ratio can be expected in the electron-density difference map. This statement was confirmed by calculating such a difference map from a simulated data set (80% complete to 2.2 Å) and of accuracy similar to that described before. The set of reflections used in this simulation actually corresponds to a data set experimentally acquired with single X-ray pulses (see §5). Phases were derived from the MbCO model of Kuriyan (Kuriyan, Wilz, Karplus &

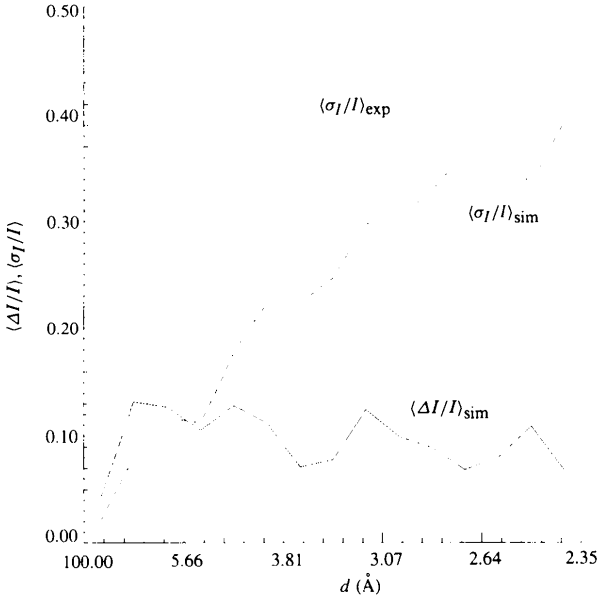

Figure 7
Simulated and measured average accuracy of singles in one MbCO Laue image compared with the expected average relative change after CO photodissociation in a 60 ps exposure. For each reflection, I is the integrated intensity from the images, ΔI is the change in intensity between the MbCO and the photodissociated Mb* images and σ_I is the standard deviation of the difference intensity. Both for the simulated and for the measured values, the 600 singles with largest I/σ_I were chosen (out of 730 recorded singles in the image).

Petsko, 1986). Only singles were used. Data were processed in exactly the same way as experimental data, using the Daresbury *Laue Software Suite* (Campbell, 1995), *CCP*4 (Collaborative Computational Project, Number 4, 1994) and the program *O* (Jones, Zou, Cowan & Kjeldgaard, 1991). As can be seen in Fig. 8, the simulated difference electron-density map clearly shows the displacement of the CO molecule from its bound position to its unligated position. However, other expected features like doming of the heme and motion of the proximal and distal histidines (Teng, Srajer & Moffat, 1994) seem to be hidden by the limited signal-to-noise ratio. Similar simulations using structure amplitudes measured at 40 K (instead of calculated from the model) also gave interpretable difference maps, although of slightly lower quality.

Although these results are encouraging, incomplete photodissociation, the presence of multiple conformations, and other sources of systematic errors were not taken into account. However, the structural changes expected at room temperature are much more extensive than those at 40 K (Teng, Srajer & Moffat, 1994), which would increase the intensity differences above those used in the simulation. If the reaction under study is reversible (as is the case with myoglobin), averaging of several repeated measurements will increase the signal-to-noise ratio, provided the crystal does not suffer from radiation damage.

We concluded from the simulation that the experiment was difficult but feasible.

5. Experimental results

BL3 is now able to acquire high-quality single-pulse Laue data sets routinely. Several experiments were performed with MbCO crystals at room temperature, with and without laser photolysis. The sample was mounted on a goniometer head and was rotated about a horizontal φ axis with a two-circle Huber diffractometer.

A first series of 19 frames covering the range 0–90° and taken 5° apart was acquired at 5 mA beam current without laser photolysis. The detector was centered on the X-ray beam, at a distance of 190 mm from the sample. The crystal size was $0.23 \times 0.4 \times 0.08\ \text{mm}^3$. Data were processed in Chicago with the package *LAUEVIEW* (Ren & Moffat, 1995*a*). Normalization of data gave a merging (unweighted) R factor of 13.5% ($I/\sigma_I > 0.5$, wavelength range used 0.35–1.6 Å) at 1.9 Å resolution, with a redundancy of 2.64. Data were processed independently at ESRF using the Daresbury *Laue/CCP*4 suite and a local integration program which performed spatial overlap deconvolution and is based on the package *IDL*, and similar results were obtained (merging R factor at 2.2 Å resolution: 13.1%). After deconvolution of multiples with *LAUEVIEW* (Ren & Moffat, 1995*b*), a completeness of 45% to 1.9 Å (66% to 2.2 Å) was obtained. The less-than-optimum completeness was largely due to the fact that a significant portion of reciprocal space had not been explored. The Laue diffraction patterns were of high quality as demonstrated by the image of Fig. 9,

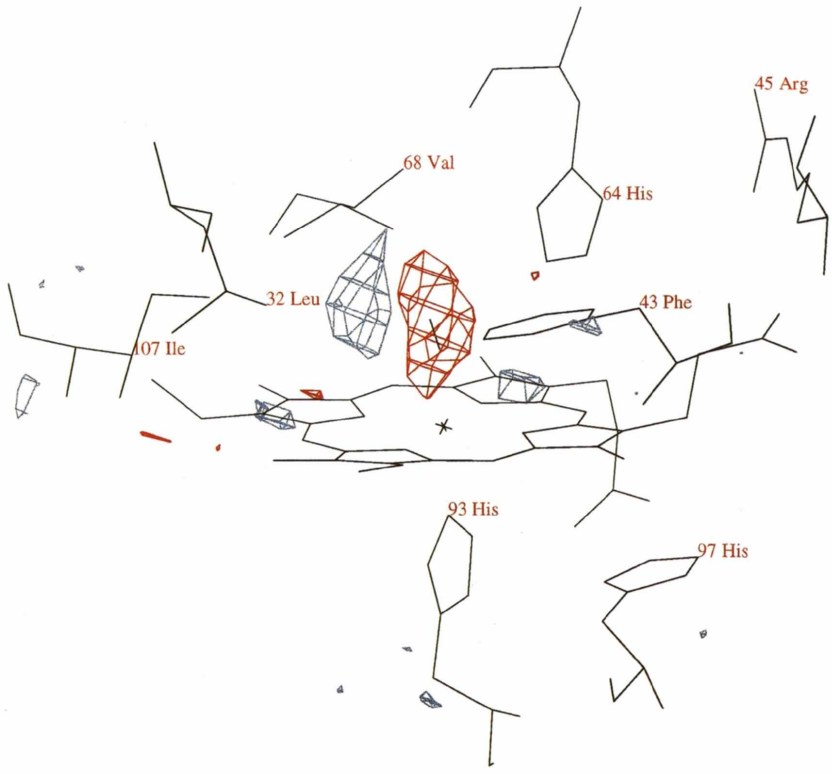

Figure 8
Simulated single-pulse electron-density difference map between MbCO and Mb*, contoured at $\pm 3\sigma$.

which contains about 800 spots with a ratio I/σ_I greater than 1.

More recently, several Laue data sets were acquired at 15 mA beam current with and without laser photolysis, and are currently being processed.

In order to assess the experimental standard deviation of measured intensities and compare them with the prediction given in §4, ten single-pulse frames were acquired under identical conditions and with the same MbCO crystal (dimensions: 0.48 × 0.4 × 0.08 mm^3) and processed independently with a resolution limit of 2.2 Å. The crystal orientation was the same as that used for the simulation of §4, Fig. 7. The experimental noise-to-signal ratio was obtained from the formula:

$$\sigma_I(\mathbf{h}, \lambda)_{\text{exp}}/I(\mathbf{h}, \lambda)_{\text{exp}} = \sigma(I_1, I_2, ..., I_{10})/I_{\text{mean}} \qquad (4)$$

where I_1, ..., I_{10} are the ten individual measurements of reflection **h**, at wavelength λ, and I_{mean} is the average value of I_1, ..., I_{10}. The results are presented in Fig. 7, and show a satisfactory agreement with the prediction. From this experiment and from the simulation of §4 we conclude that a clear signal in the experimental difference density maps can be expected from data of the quality currently being processed.

6. Conclusions

We have highlighted the ability to record routinely high-quality single-pulse Laue images from protein crystals at ESRF. Although only careful processing of real data will provide a firm conclusion as to whether or not one can observe structural modifications in macromolecular crystals on such a short timescale, simulations are very encouraging and justify the heavy instrumental work required by the technique. This instrumentation has been successfully developed, and full Laue data sets were acquired in the single-pulse mode on MbCO crystals.

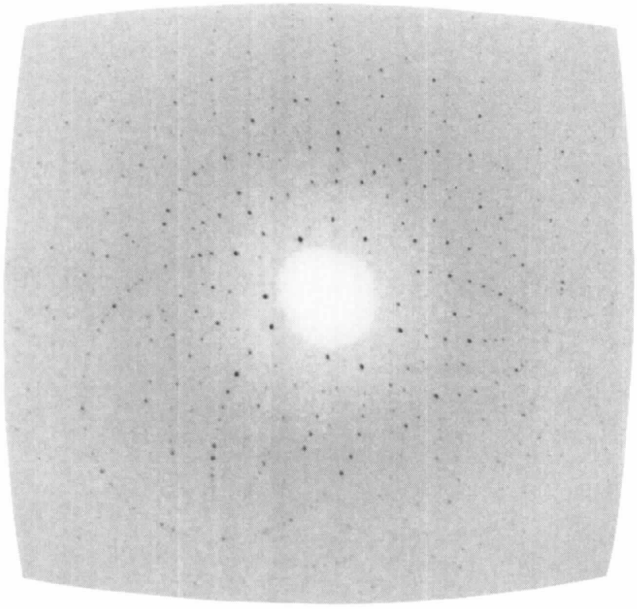

Figure 9
A 60 ps Laue image of an MbCO crystal. The crystal diffracted up to 1.9 Å (see text).

This research was supported by grants from the W. M. Keck Foundation and the National Institutes of Health to KM. We thank J. P. Moy, M. Hanfland and D. Häusermann for their assistance in performing the experiments and C.-I. Brändén and the ESRF machine division for their support. J. Richou and Y. Schertz (University of Toulon, IFREMER) are acknowledged for providing the laser/fiber coupling set-up.

References

Bartunik, H. D. (1983). *Nucl. Instrum. Methods*, A**208**, 523–533.
Bolduc, J. M., Dyer, D. H., Scott, W. G., Singer, P., Sweet, R. M., Koshland, D. E. & Stoddard, B. L. (1995). *Science*, **268**, 1312–1318.
Bourgeois, D., Ursby, T., Wulff, M., Pradervand, C., Legrand, A., Schildkamp, W., Labouré, S., Srajer, V., Teng, T. Y., Roth, M. & Moffat, K. (1995). *SPIE Proc.* **2521**, 178–181.
Campbell, J. W. (1995). *J. Appl. Cryst.* **28**, 228–236.
Clifton, I. J., Fülop, V., Hadfield, A. T., Nordlund, P., Andersson, I. & Hajdu, J. (1991). *Nucl. Instrum. Methods*, A**303**, 476–487.
Collaborative Computational Project, Number 4 (1994). *Acta Cryst.* D**50**, 760–763.
Cruickshank, D. W. J., Helliwell, J. R. & Johnson, L. N. (1992). *Time-Resolved Macromolecular Crystallography*. Oxford: Oxford Science Publications.
Franzen, S., Bohn, B., Poyart, C. & Martin, J. L. (1995). *Biochemistry*, **34**, 1224–1237.
Fülop, V., Phizackerley, R. P., Soltis, S. M., Clifton, I. J., Wakatsuki, S., Erman, J., Hajdu, J. & Edwards, S. L. (1994). *Structure*, **2**, 201–208.
Hagen, S. J., Hofrichter, J. & Eaton, W. A. (1995). *Science*, **269**, 959–962.
Hajdu, J. & Andersson, I. (1993). *Annu. Rev. Biophys. Biomol. Chem.* **22**, 467–498.
Hajdu, J., Machin, P. A., Campbell, J. W., Greenhough, T. J., Clifton, I. J., Zurek, S., Gover, S., Johnson, L. N. & Elder, M. (1987). *Nature (London)*, **329**, 178–181.
Hammersley, A. P., Svensson, S. O. & Thompson, A. (1994). *Nucl. Instrum. Methods*, A**346**, 312–321.
Helliwell, J. R., Habash, J., Cruickshank, D. W. J., Harding, M. M., Greenhough, T. J., Campbell, J. W., Clifton, I. J., Elder, M., Machin, P. A., Papiz, M. Z. & Zurek, S. (1989). *J. Appl. Cryst.* **22**, 483–497.
Jones, T. A., Zou, J.-Y., Cowan, S. W. & Kjeldgaard, M. (1991). *Acta Cryst.* A**47**, 110–119.
Kishimoto, S. (1991). *Nucl. Instrum. Methods*, A**309**, 603–605.
Kuriyan, J., Wilz, S., Karplus, M. & Petsko, G. A. (1986). *J. Mol. Biol.* **192**, 133–154.
LeGrand, A. D., Pradervand, C. & Schildkamp W. (1996). In preparation.
LeGrand, A. D., Schildkamp, W. & Blank, B. (1989). *Nucl. Instrum. Methods*, A**275**, 442–446.
Lim, M., Jackson, T. A. & Anfinrud, P. A. (1995). *Science*, **269**, 962–966.
Mills, D. M. (1991). *Handbook on Synchrotron Radiation*, Vol. 3, pp. 291–335. Amsterdam: Elsevier.
Mills, D. M., Larson, B. C., White, C. W. & Noggle, T. S. (1983). *Nucl. Instrum. Methods*, A**208**, 511–517.

Mills, D. M., Lewis, A., Harootunian, A., Huang, J. & Smith, B. (1984). *Science*, **223**, 811–813.
Moffat, K. (1989). *Annu. Rev. Biophys. Biophys. Chem.* **18**, 309–332.
Moffat, K., Chen, Y., Ng, K., McRee, D. & Getzoff, E. D. (1992). *Philos. Trans. R. Soc. London Ser. A*, **340**, 175–190.
Moffat, K. & Henderson, R. (1995). *Curr. Opin. Struct. Biol.* **5**, 656–663.
Moffat, K., Szebenyi, D. & Bilderback, D. (1984). *Science*, **223**, 1423–1425.
Moy, J. P. (1994). *Nucl. Instrum. Methods*, A**348**, 641–644.
Moy, J. P., Hammersley, A. P., Svensson, S. O., Thompson, A., Brown, K., Claustre, L., Gonzalez, A. & McSweeney, S. (1996). *J. Synchrotron Rad.* **3**, 1–5.
Pai, E. F. (1992). *Curr. Opin. Struct. Biol.* **2**, 821–827.
Ren, Z. & Moffat K. (1994). *J. Synchrotron Rad.* **1**, 78–82.
Ren, Z. & Moffat, K. (1995*a*). *J. Appl. Cryst.* **28**, 461–468.
Ren, Z. & Moffat, K. (1995*b*). *J. Appl. Cryst.* **28**, 482–494.
Schlichting, I., Almo, S. C., Rapp, G., Wilson, K., Petratos, K., Lentfer, A., Wittinghofer, A., Kabsch, W., Pai, E. F., Petsko, G. A. & Goody, R. S. (1990). *Nature (London)*, **345**, 309–315.
Schlichting, I., Berendzen, J., Phillips, G. N. Jr & Sweet, R. M. (1994). *Nature (London)*, **371**, 808–812.
Singer, P. T., Smalås, A., Carty, R. P., Mangel, W. F. & Sweet, R. M. (1993). *Science*, **259**, 669–673.
Szebenyi, D. M., Bilderback, D. H., LeGrand, A., Moffat, K., Schildkamp, W., Smith Temple, B. & Teng, T. (1992). *J. Appl. Cryst.* **25**, 414–423.
Teng, T. Y., Srajer, V. & Moffat, K. (1994). *Nature Struct. Biol.* **1**, 701–705.
Warren, B. E. (1969). *X-ray Diffraction*. Reading: Addison-Wesley.
Weisgerber, S. & Helliwell, J. R. (1993). *J. Chem. Soc. Faraday Trans.* **89**(15), 2667–2675.
Wulff, M. (1992). *SPIE Proc.* **1739**, 576–591.